

Cite this: *J. Mater. Chem. A*, 2024, **12**, 22945

# Exploring the potential of MB<sub>4</sub> (M = Cr, Mo, and W) MBenes as high-capacity anode materials for Ca-ion batteries: a DFT approach†

M. Kashif Masood,<sup>a</sup> Jing Wang,<sup>✉</sup> Juntao Song<sup>a</sup> and Ying Liu<sup>ab</sup>

Two-dimensional MBene monolayers can be used in rechargeable metal-ion batteries because of their layered structure, abundant accommodating sites and high specific surface area. Owing to the abundant resources and cost effectiveness of calcium, calcium ion batteries (CIBs) are a suitable alternative to Li-ion batteries (LIBs). In this study, the performance of MB<sub>4</sub> (M = Cr, Mo, and W) monolayer MBenes as an anode material for calcium ion batteries has been predicted via a density functional theory approach. We found that these monolayers have a thermally, mechanically, and dynamically stable structure. Furthermore, the lightweight properties and energetically favorable adsorption of 6 layers of Ca atoms endow CrB<sub>4</sub>, MoB<sub>4</sub> and WB<sub>4</sub> with high storage capacities of 3377 mA h g<sup>-1</sup>, 2311 mA h g<sup>-1</sup> and 1416 mA h g<sup>-1</sup>, as well as comparatively low average open circuit voltage of 0.45 V, 0.47 V and 0.35 V, respectively. This reveals their notable superiority over most 2D anode materials. Likewise, the faster mobility of Ca ions in the MB<sub>4</sub> monolayer was proved by low activation barriers values of 0.67 eV, 0.72 eV and 0.79 eV for CrB<sub>4</sub>, MoB<sub>4</sub> and WB<sub>4</sub>, respectively. Additionally, the metallic nature of the materials remained well maintained after the adsorption of full concentrations of Ca ions. These properties signify that monolayers CrB<sub>4</sub>, MoB<sub>4</sub> and WB<sub>4</sub> are promising anode materials for CIBs with commendable rate capacities.

Received 1st April 2024  
Accepted 5th July 2024

DOI: 10.1039/d4ta02176b

rsc.li/materials-a

## 1 Introduction

In recent decades, Li-ion batteries (LIBs) have appeared as the primary means of converting and storing electrical energy. High energy-density and less expensive energy-storage devices are necessary, nevertheless, because of the quick development of commercial electric vehicles (EVs) and large scale grid energy storage.<sup>1,2</sup> However, another obstacle to the quick development of LIBs is the inadequate lithium reserves in nature, which raises the price of LIBs.<sup>3,4</sup> Therefore, it becomes crucial from an intellectual and scientific standpoint to develop next-generation batteries that use ions other than Li ions as a charge carrier called non-Li metal ions.<sup>5</sup> Non-Li metal-ion batteries (NLMIBs) have thus far been the subject of much research and have gained attention from the academic community. Examples of NLMIBs include Na-, K-, Mg-, Ca-, and Al-ion batteries. Because of their high valence state and light weight, some of these NLMIBs may have greater theoretical capacities since they employ multivalent metal-ions such as Mg<sup>2+</sup>, Ca<sup>2+</sup>, and Al<sup>3+</sup>.<sup>6–10</sup> More significantly, in comparison to Li, all these metal ions are

easily available in the earth's crust. It is imperative to develop and seek out high-efficiency electrode materials to expedite the advancement of NLMIBs, although bulk materials have been examined and reported for the use of high capacity electrode materials for NLMIBs, such as monolayered transition-metal oxides<sup>11</sup> and polyanion compounds.<sup>12</sup>

The large ionic radius of non-Li metal ions and augmented coulombic attractions towards multivalent ions impede their rate performance.<sup>13</sup> Because they are inexpensive, non-toxic, and readily available, calcium-ion batteries (CIBs) are seen as appropriate substitutes to lithium-ion batteries. CIBs are starting to emerge as the rechargeable battery technology of the future.<sup>14</sup> For next-generation electrochemical applications, CIBs may be a better choice than LIBs due to the following advantages: (a) the divalent character, which promotes stronger bonding and storage of one electron for lithium and two for each Ca-atom, which results in an increased theoretical volume and specific capacity; (b) natural abundance;<sup>15</sup> (c) calcium may be electrodeposited smoothly without any dendritic development problems that are cause in metallic lithium; (d) because of its lower radius, diffusion is more rapid than that of lithium ions.<sup>16</sup> The metal ion batteries' performance is also significantly impacted by the selection of materials used for the anode of the batteries. Li-ion batteries predominantly employ graphite as their negative electrode material, characterized by the modest theoretical capacity of 372 mA h g<sup>-1</sup>, which prevents it from

<sup>a</sup>Department of Physics and Hebei Advanced Thin Film Laboratory, Hebei Normal University, Shijiazhuang 050024, China. E-mail: jwang@hebtu.edu.cn

<sup>b</sup>National Key Laboratory for Materials Simulation and Design, Beijing 100083, China

† Electronic supplementary information (ESI) available. See DOI: <https://doi.org/10.1039/d4ta02176b>

being developed further for energy storage purposes.<sup>17,18</sup> Therefore, to remedy this condition, new anode materials are desperately needed. In this context, two-dimensional (2D) materials offer greater space for these massive metal ions and a smooth surface structure that facilitates the multivalent ions' rapid diffusion, removing the constraint present in bulk materials.<sup>19,20</sup>

Two-dimensional (2D) materials possess a large surface area, exceptionally fast electron mobility, and superior mechanical qualities<sup>21,22</sup> that are particularly interesting as anode materials for LIBs and NIBs.<sup>23</sup> A 2D electrode material for LIBs that has been demonstrated thus far is graphene.<sup>24,25</sup> Novel 2D materials have since been researched as potential anode materials for metal ion batteries. These materials include silicene,<sup>26</sup> phosphorene,<sup>27,28</sup> borophene,<sup>29,30</sup> boron phosphide,<sup>31</sup> Mo<sub>2</sub>C,<sup>32</sup> and 2D transition metal carbides or nitrides, known as MXenes.<sup>33,34</sup> The selective etching of A atoms from MAX phases using hydrofluoric acid (HF) at room temperature can be used to synthesize MXenes.<sup>33,34</sup> Guo *et al.*<sup>35</sup> looked into novel 2D transition metal borides (TMBs) for LIBs. It has been determined that in comparison to the most popular graphite anode (372 mA h g<sup>-1</sup> and 0.3–0.5 eV), many 2D materials offer a much higher energy storage capacity (theoretical capacity of >400 mA h g<sup>-1</sup>) and fast ion diffusion dynamics (diffusion energy barrier height of <0.1 eV) for Li ion batteries. MBenes are a broad class of two-dimensional materials that are synthesized similarly to MXenes and are typically formed from transition metal borides.<sup>36–39</sup> A valence electron deficiency state in the related crystal structures is promoted by the boron-rich chemical environment of MBenes, which results in strong contacts between the metal ions and the electrode materials. Through the use of first principles calculations, it was determined that Cr<sub>2</sub>B<sub>2</sub>, Fe<sub>2</sub>B<sub>2</sub>, Mo<sub>2</sub>B<sub>2</sub>, and W<sub>2</sub>B<sub>2</sub> were the four types of MBenes that were anticipated to be formed from Cr<sub>2</sub>AlB<sub>2</sub>, Fe<sub>2</sub>AlB<sub>2</sub>, MoAlB, and WAlB through selective etching techniques. The synthesis of 2D Mo<sub>2</sub>B<sub>2</sub> and Cr<sub>2</sub>B<sub>2</sub> was successfully done by these techniques. The applications and extensive research on MBenes has been made possible by the previous findings.<sup>40,41</sup>

A multi-layer adsorption mechanism for metal ions is expected to be supported by the improved chemical interactions between the MBenes and the electron donors (alkaline or alkaline earth metal), leading to an ultra-high ion storage capacity (>1000 mA h g<sup>-1</sup>). Indeed, the adsorption mechanism of alkaline (earth) metal ions on MBenes has been confirmed by several earlier density functional theory-based theoretical computations. Jia and coworkers<sup>39</sup> anticipated the electrochemical characteristics of several type MBenes, such as V<sub>2</sub>B<sub>2</sub>, Cr<sub>2</sub>B<sub>2</sub>, Mn<sub>2</sub>B<sub>2</sub>, Ti<sub>2</sub>B<sub>2</sub>, Zr<sub>2</sub>B<sub>2</sub>, and Nb<sub>2</sub>B<sub>2</sub>, for alkaline metal ion batteries. The extraordinary qualities of these materials like outstanding electronic conductivity, large surface area, different types of crystal structures make them good for energy storage and conversion applications.<sup>42–46</sup> To investigate the suitability of the 2D boron sheet borophene as an electrode material for MIBs, various research has been conducted on the Ag (111) substrate. The storage capacities of Li, Na, K, Mg and Ca ions and their adsorption behavior are studied on the different monolayers of boron-based materials, and it was found that the

boron-based materials can be the best choice as anode materials in the metal ion batteries. Yang *et al.* studied CrB, MnB, FeB, SrB<sub>8</sub> and TiB<sub>4</sub> for the Li-, Na-, K-, Mg- and Ca-ion batteries.<sup>47,48</sup> Research has shown that monolayer TiB has storage capabilities of 408.421 mA h g<sup>-1</sup> for Li ions and 328.162 mA h g<sup>-1</sup> for Na ions, respectively. These results underline the material's potential for use in energy storage applications.<sup>49</sup> Monolayer Ti<sub>2</sub>N has demonstrated notable capacities, with 484 mA h g<sup>-1</sup> for Li ions and 242 mA h g<sup>-1</sup> for K ions recorded.<sup>50</sup> The capacity of 439 mA h g<sup>-1</sup> for Li ions, 348 mA h g<sup>-1</sup> for Na ions, and 141 mA h g<sup>-1</sup> for K ions are demonstrated by monolayer Ti<sub>2</sub>C.<sup>51</sup> The capacity of monolayer TiB<sub>4</sub> for Li ions is 510.534 mA h g<sup>-1</sup>, for Na ions is 390.999 mA h g<sup>-1</sup>, and for K ions is 316.59 mA h g<sup>-1</sup>, which are encouraging.<sup>52</sup> For Mg-ion on Sc<sub>2</sub>B, V<sub>2</sub>B and Ti<sub>2</sub>B, the M<sub>2</sub>B phases exhibit ultra-high specific capacities of 3192.813 mA h g<sup>-1</sup>, 2853.953 mA h g<sup>-1</sup> and 3018.414 mA h g<sup>-1</sup>, respectively.<sup>53</sup> TiB<sub>4</sub> has a Ca storage capacity of 1176 mA h g<sup>-1</sup>, and SrB<sub>8</sub> has a Ca storage capacity of 616 mA h g<sup>-1</sup>.<sup>47</sup>

Inspired by the previous investigations, we selected the first three elements of group VI and designed the MB<sub>4</sub>(Cr, Mo, W) using the computational structure prediction method in the framework of density functional theory. To determine the possibility of monolayer MBenes (CrB<sub>4</sub>, MoB<sub>4</sub>, and WB<sub>4</sub>) with dynamic stability and an electronic configuration as anode materials, we investigated these materials. It was also thoroughly studied how the monolayer MBenes behaved in terms of adsorption, diffusion barriers, maximum theoretical capacity, and average open-circuit voltage. According to the test findings, these monolayer MBenes show promise as cathode/anode materials.

## 2 Computational detail

In this study, advanced computational tools were used to explain the behavior of the materials for CIBs under different conditions. The well-known Vienna *ab initio* simulation package (VASP) was employed for their adaptability and precision in the simulating the complex system at the atomic scale and was conducted by the use of various density functional theory (DFT) frameworks.<sup>54,55</sup> To understand the material structure stability and dynamic behavior, the study effectively recorded the complex interactions of the electrons and ions within the materials using the plane-wave approach with cutoff energy of 550 eV. These values were determined through a convergence test of cutoffs based on the total energy, as shown in Fig. S1.† The exchange–correlation energy is represented by the Perdew, Burke, and Ernzerhof (PBE) functional,<sup>56,57</sup> 12 × 12 × 1 *k*-points were used for geometry optimization and 5 × 5 × 1 Monkhorst-Pack *k*-points was used for the 3 × 3 × 1 supercell of MB<sub>4</sub>, assuring a thorough investigation of the phase space of the materials. A vacuum space of 18 Å was introduced for both CrB<sub>4</sub> and MoB<sub>4</sub>, while it was 20 Å for WB<sub>4</sub> to investigate the interactions between the neighboring layers. The convergence test was also employed to determine the *k*-points and vacuum space, as shown in Fig. S2–S4.† GGA-PBE was utilized for electronic structure calculations, followed by the HSE06 hybrid

density functional method to delve deeper into the material's electronic properties and analyze its band structure.<sup>58,59</sup> The DFT-D3 approach was used for the consideration of long-range van der Waals interactions.<sup>60,61</sup> Density functional perturbation theory (DFPT) was used to investigate the dynamical stability of the studied materials, and PHONOPY code was used to investigate the phonon characteristics.<sup>62</sup> The convergence criteria were thoroughly specified at  $-0.02$  eV  $\text{\AA}^{-1}$  established at Hellmann–Feynman force and a total energy value of  $10^{-8}$  eV, which promised reliability and precision of the phonon computations. Charge transfer from the Ca-ion to the  $\text{CrB}_4$ ,  $\text{MoB}_4$  and  $\text{WB}_4$  monolayer was performed by the Bader charge analysis that provides the charge pathway through the materials. Moreover, the structure stabilities and adsorption of Ca-ion layers on the studied materials for anode *ab initio* molecular dynamic simulations (AIMD) was carried out at 300 K (room temperature) over the 5 ps time scale, which provides an insight into behaviors of the materials' structure at room temperature.<sup>60,61</sup> VASPKIT code was used for the analysis and interpretation of the various simulation results of pre and post processing of a vast amount of data.<sup>63</sup> Furthermore, the dynamical and structural characteristics of the studied materials were investigated under the mechanical parameters, and the phonon frequency was discovered by the Hellman and Feynman theorem with the direct supercell approach, which provides important information about the vibrational properties of the studied materials.<sup>64</sup> Mechanical parameters like Poisson's ratio and Young's modulus were investigated using the Voigt–Reuss–Hill approximation, and the values of elastic constants were examined using the stress-tensor-created small strain, which provides resilience and mechanical robustness to the materials.<sup>65</sup> Finally, the charging and discharging processes were investigated using the simulation of surface barriers and minimum energy paths (MEPs) of Ca migration in the  $\text{MB}_4$  monolayer with the climbing nudged elastic band (CI-NEB) method. This technique approximately justifies Ca-ion batteries' calcium intercalation/deintercalation mechanisms.<sup>66,67</sup>

## 3 Results and discussions

### 3.1 Structure of the $\text{MB}_4$ monolayer

To check the suitability of the material for the calcium ion batteries, it is important to check the behavior of Ca atoms on that material. This structure of the material is important; Fig. 1(a) shows the general structure of 2D monolayer  $\text{MB}_4$  ( $M = \text{Cr}, \text{Mo}, \text{and W}$ ), and their optimized side view of structures are shown in Fig. 1(b–d), while Fig. S5(a–c)† represents the top view of the optimized structures of  $\text{CrB}_4$ ,  $\text{MoB}_4$  and  $\text{WB}_4$ , respectively. The Cr/Mo/W layer is sandwiched between two layers of B atoms, the unit cell has four B atoms and one Cr/Mo/W atom, and there is an intermediate triangular layer that is composed of the Cr/Mo/W atom between the two hexagonal sheet of B atoms. These monolayers have 1 : 4 ratio of B atoms to the Cr/Mo/W atom. After the geometry optimizations of the  $3 \times 3 \times 1$  supercell of  $\text{MB}_4$ , the lattice constant and thickness ( $d$ ) for  $\text{CrB}_4$  were found to be 8.67  $\text{\AA}$  and 3.02  $\text{\AA}$ , 8.87  $\text{\AA}$  and 3.28  $\text{\AA}$  for  $\text{MoB}_4$ , and 8.88  $\text{\AA}$  and 3.30  $\text{\AA}$  for  $\text{WB}_4$ , which are similar to the

previous report on these materials.<sup>68–72</sup> Because the W atom has a larger atomic size than those of Cr and Mo,  $\text{WB}_4$  has larger lattice parameters than  $\text{CrB}_4$  and  $\text{MoB}_4$ . One unstable boron atom was located next to the carbon atom sheet in the periodic table. In order to accomplish a completely filled  $\pi$ -bond within the honeycomb, one extra electron is needed for each boron atom, resulting in the  $2s^2 2p^2$  configuration.

The structural stability of boron sheet can be obtained by adding atoms of group VI (like Cr, Mo and W), which involve the two boron-sheets, and the  $\text{B}^-$  anion has the same configuration as the B atom in the structure of graphene since each atom has the potential to contribute four electrons, creating the  $2s^2 2p^2$  electrical structure. Every B honeycomb is stabilized by the  $\sigma$ -bonds that is formed by  $sp^2$  hybrid orbitals, while the  $\sigma$ -bonds between  $\text{B}^-$  anions are formed by the pz orbitals. It is stable and resembles graphene because the B atoms form covalent bonds with other B atoms and ionic bonds with the remaining atoms (Cr/Mo/W). Inside these monolayers, the movement of the high-charge impact is influenced by strong van der Waals (vdW) forces between the two boron sheets, which results in the development of a double Dirac cone. Two Dirac cones appear in the energy window shown in Fig. S6(a–c),† close to the Fermi level.<sup>68–70</sup> Two symmetry cones are visible in the electronic structure: cone I is situated at K, which is above the Fermi level, and cone II is located at the  $\Gamma$  to the K site just below the Fermi level, which shows the metallic behavior of  $\text{MB}_4$ . In agreement with earlier research, both cones have the Fermi velocities of  $5.31 \times 10^5 \text{ ms}^{-1}$ , or about half that of graphene.<sup>73–75</sup> The energy band structures of 2D monolayer  $\text{CrB}_4$ ,  $\text{MoB}_4$ , and  $\text{WB}_4$  exhibit distinct energy bands through the Fermi level. When employing the HSE06 method for electronic structure calculations, the investigated material retained its metallic character. Despite the increased accuracy provided by the HSE06 functional, the system's electronic configuration did not exhibit a bandgap, indicating its continued metallic behavior, as shown in Fig. S7(a–c).† This indicates that the  $\text{MB}_4$  materials are very suitable for use as electrode materials in Ca-ion batteries because of their metallic conductivity.

Material stability was evaluated when we examined their dynamic stability with an emphasis on the dynamic stability of  $\text{MB}_4$ . The phonon dispersion curve and projected vibrational density of states (PVDOS) for the monolayers  $\text{MoB}_4$ ,  $\text{CrB}_4$ , and  $\text{WB}_4$  are presented in Fig. 1(e–g), respectively. Positive frequencies are indicative of favorable dynamic stability in all the three materials. We also performed the phonon calculations to check the further dynamical stabilities of both materials under the strain of +2.5% and –2.5% and found no imaginary frequencies, as shown in Fig. S8(a–c) and S9(a–c).† The mechanical stability of the materials used to produce high-capacity anodes must be considered. Batteries must have strong mechanical properties to withstand volume growth caused by charge–discharge cycles because they do not collapse under extreme pressure or stress like other 2D electrode materials do.<sup>76,77</sup> We calculated the in-plane stiffness constants to assess the mechanical stability of anode materials. For a two-dimensional case of material under stress, the Voigt notations

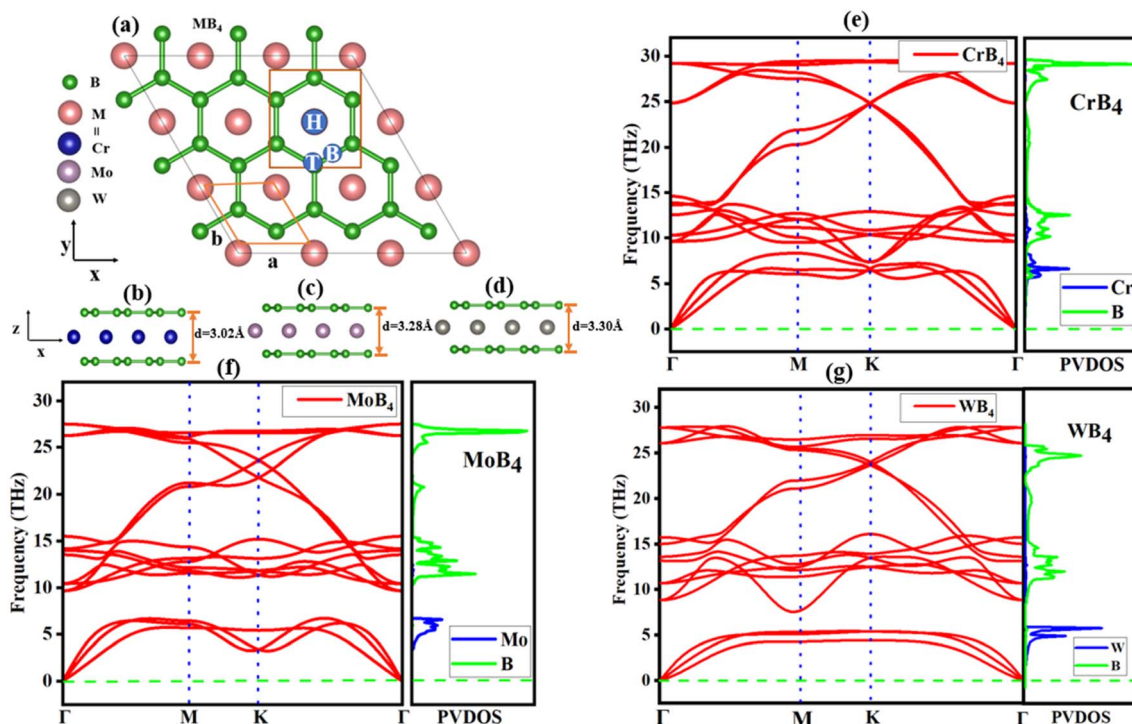


Fig. 1 (a) Top view of the  $MB_4$  structure with three stable sites (H, T, and B sites). (b–d) Side view and (e–g) phonon dispersion curve of  $CrB_4$ ,  $MoB_4$  and  $WB_4$ .

1 –  $xx$ , 2 –  $yy$ , and 6 –  $xy$ ,<sup>78</sup> the total PE  $U(\epsilon)$  can be written as follows.<sup>79</sup>

$$U(\epsilon) = \frac{1}{2}C_{11}\epsilon_{xx}^2 + \frac{1}{2}C_{22}\epsilon_{yy}^2 + C_{12}\epsilon_{xx}\epsilon_{yy} + 2C_{66}\epsilon_{xy}^2 \quad (1)$$

In eqn (1),  $C_{11}$ ,  $C_{12}$ ,  $C_{22}$ , and  $C_{66}$  are the dimensional elastic-tensor and elastic constants, where  $C_{11}$  represents the materials stiffness when the applied strain is along the  $x$ -axis and  $C_{12}$  represents the stiffness when the applied strain is along the  $y$ -axis. The capability of the  $MB_4$  material to endure biaxial strain is represented by  $C_{22}$  and the resistance to distortion cause because of the share strain is represented by  $C_{66}$ , while  $\epsilon_{xx}$  and  $\epsilon_{yy}$  represent the uniaxial strain along the  $x$ - and  $y$ -axis, respectively. A methodology similar to that of Barik and Pal was employed, subjecting the material to stresses ranging from  $-2.5\%$  to  $+2.5\%$  with a tiny interval of  $0.5\%$ .<sup>80,81</sup> A 2nd order polynomial was fitted to the uniaxial deformation along  $x$ - and the  $y$ -axes in order to acquire the strain-energy facts arising from the values of  $C_{11}$  and  $C_{22}$ . Similarly, as shown in Fig. S10(a–c),<sup>†</sup> biaxial planar distortion along the  $xy$ -plane yielded the  $C_{12}$  value, where  $C_{11}$  and  $C_{22}$  are equal in the hexagonal system, and an additional relation  $C_{66} = \frac{1}{2}(C_{11} - C_{12})$  holds.

Elastic constants values allow for the direct determination of in-plane Poisson's ratio ( $\nu$ ) and Young's modulus ( $Y$ ),<sup>82</sup> and we can calculate the values with these formula with elastic constant, *i.e.*, Poisson's ratio ( $\nu$ ) =  $\frac{C_{12}}{C_{11}}$  and Young's modulus ( $Y$ ) =  $\frac{C_{11}^2 - C_{12}^2}{C_{11}}$ . A material's response to mechanical deformation is known as elastic instability, and it is correlated with

its elastic constants. When many elastic constants exhibit  $-ve$  response, it suggests a potential transition of phase or instability of the structure and shows that the crystal structure is no more stable to insignificant deformation; thus, this instability develops. The calculated values of the elastic constant of the materials are shown in Table 1; all these elastic constants followed the Born–Huang<sup>83,84</sup> conditions of stability of the materials, which is  $C_{11}C_{12} > 0$ ,  $C_{11}C_{22} - C_{12}C_{12} > 0$ ,  $C_{11} > C_{12}$ , and no value of the elastic constant is negative, which means that all the monolayers are mechanically stable.<sup>80,85</sup> The values of Poisson's ratio and Young's modulus showed a notable degree of flexibility of the materials, and our calculated values are greater than that of some other 2D monolayer materials reported in the literature, *i.e.*,  $SiP_3$ ,<sup>86</sup> 2D-SnB<sup>87</sup> and  $B_2N_2$ .<sup>88</sup> The systematic investigation of the mechanical and physical characteristics yields useful information that advances the manufacture of flexible anode materials for Ca-ion batteries.

### 3.2 Adsorption of Ca on $MB_4$ monolayer

The adsorption mechanism of Ca on the  $MB_4$  monolayer is governed by the energy surface of the  $CrB_4$ ,  $MoB_4$  and  $WB_4$

Table 1 Calculated elastic constants ( $N\ m^{-1}$ ), Young's modulus ( $N\ m^{-1}$ ) and Poisson's ratio for  $CrB_4$ ,  $MoB_4$  and  $WB_4$

Material	$C_{11}$	$C_{12}$	$C_{66}$	Young's modulus ( $Y$ )	Poisson's ratio ( $\nu$ )
$CrB_4$	356.26	84.01	136.13	336.45	0.24
$MoB_4$	402.12	58.05	172.04	391.16	0.14
$WB_4$	407.76	61.32	173.22	398.53	0.15

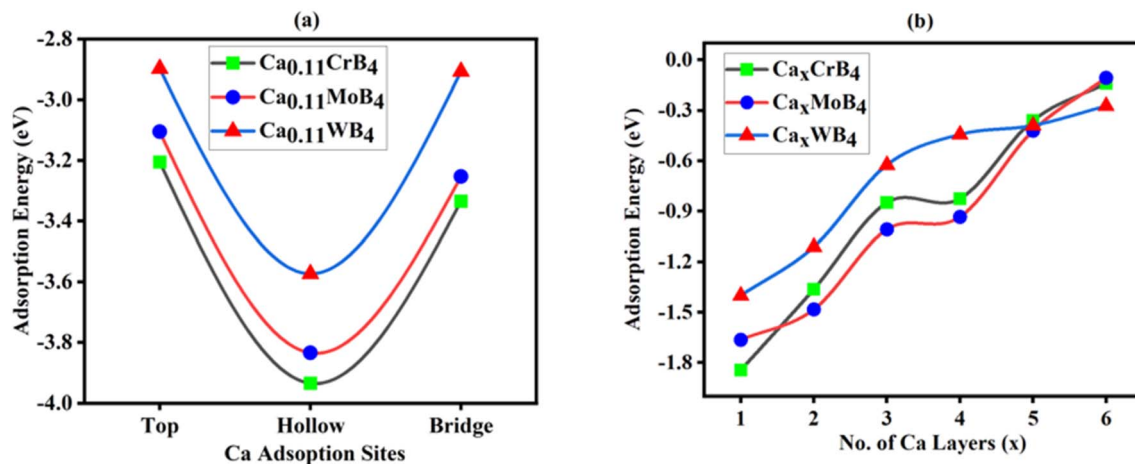


Fig. 2 Adsorption energies ( $E_{\text{ads}}$ ) of CrB<sub>4</sub>, MoB<sub>4</sub> and WB<sub>4</sub>. (a) Stable Ca-sites with their respective adsorption energies and (b) average adsorption energies ( $E_{\text{ad}}$ ) with increasing Ca-adsorbed layers ( $x = 1, 2, 3, 4, 5$ , and 6).

monolayers. Firstly, we calculated the adsorption energy of single Ca-atom on different possible sites on the surface of the MB<sub>4</sub> anode material, and these sites are shown in Fig. 1(a). According to the structure symmetry, we selected the three different adsorption sites, which are labeled as Hollow-site (H-site), Bridge-site (B-site) and Top-site (T-site). Adsorption is only suitable when the material has suitable stable sites; for this purpose, checking the adsorption energy of respective sites is very important for Ca-atom adsorption on the surface of the MB<sub>4</sub> monolayer. For this, we computed the adsorption energy of each site and compared it using the following equation for the adsorption of a single Ca atom.<sup>89</sup>

$$E_{\text{ads}} = (E_{\text{Ca-MB}_4} - E_{\text{MB}_4} - E_{\text{Ca}}) \quad (2)$$

In the above equation, the total energy of the MB<sub>4</sub> surface with one Ca atom adsorbed is represented by  $E_{\text{Ca-MB}_4}$ , and  $E_{\text{MB}_4}$  represents the total energy of pure MB<sub>4</sub>, while  $E_{\text{Ca}}$  denotes the total energy of a single Ca-atom. The adsorption energies of all these three sites are tabulated in Table 2 and graphically represented in Fig. 2(a), which represents that all values of adsorption energies are negative, which is favorable of the adsorption of Ca atom on the MB<sub>4</sub> surface and shows

exothermic adsorption, which is the most common form of the metallic cluster. Metallic clusters in calcium-ion batteries improve ion adsorption, diffusion, stability, and conductivity, thereby enhancing the battery performance. The calculated adsorption energies values are  $-3.94$  eV,  $3.18$  eV and  $-2.74$  eV for the Hollow site;  $-3.93$  eV,  $-3.27$  eV and  $-2.69$  eV for the Bridge site; and  $-3.20$  eV,  $-2.33$  eV and  $-1.89$  eV for the Top site of CrB<sub>4</sub>, MoB<sub>4</sub> and WB<sub>4</sub>, respectively. It can be seen that the adsorption energies of the Hollow site are more negative as compared to the T- and B-site for all three materials, which indicates that the H-site is the most stable site and is favorable for the further adsorption of Ca atom.

After finding the suitable site for adsorption, it is significant to find the interaction behavior of Ca atom on the surface of CrB<sub>4</sub>, MoB<sub>4</sub> and WB<sub>4</sub> monolayers. For this reason, we studied the charge exchange between the Ca-ion and these monolayers. Bader charge analysis is a technique that can be used to combine the electrons around an atom with its chemical valence, enabling the analysis of charge transfer between the Ca atom and the MB<sub>4</sub> monolayer before and after the adsorption process, which was used to study whether or not the adsorption process is favorable between Ca and the MB<sub>4</sub> monolayer. For the most stable H-site, Ca atom transferred  $1.40e$  to the monolayer

Table 2 Calculated adsorption energy, Bader charge and structural parameters for Ca atoms on both sides of CrB<sub>4</sub>, MoB<sub>4</sub> and WB<sub>4</sub>

Parameters	Adsorption energy (eV)			Bader charge (e)		
	Top	Bridge	Hollow	Top	Bridge	Hollow
Ca <sub>0.11</sub> CrB <sub>4</sub>	-3.20	-3.93	-3.94	1.39	1.38	1.40
Ca <sub>0.11</sub> MoB <sub>4</sub>	-2.33	-3.17	-3.18	1.31	1.30	1.32
Ca <sub>0.11</sub> WB <sub>4</sub>	-1.89	-2.69	-2.74	1.34	1.34	1.35
Height ( $h_{\text{s-s}}$ ) of CrB <sub>4</sub>	3.02 Å					
Height ( $h_{\text{s-s}}$ ) of MoB <sub>4</sub>	3.28 Å					
Height ( $h_{\text{s-s}}$ ) of WB <sub>4</sub>	3.30 Å					
Lattice constants ( $a, b$ ) of CrB <sub>4</sub>	8.67 Å					
Lattice constants ( $a, b$ ) of MoB <sub>4</sub>	8.87 Å					
Lattice constants ( $a, b$ ) of WB <sub>4</sub>	8.88 Å					

CrB<sub>4</sub>, 1.32e to the monolayer MoB<sub>4</sub> and 1.35e to the monolayer WB<sub>4</sub>. The charge of the Ca atom transferred from the other adsorption sites to these monolayers with the respective adsorption energies is tabulated in Table 2. The charge transferred values of these sites indicates the strength of strong adsorption, which shows robust chemical interactions between the Ca atom and the material surface, promoting adsorption and increasing the theoretical capacity.<sup>90,91</sup> In a calcium-ion battery, calculating the charge density difference (CDD) when Ca adsorbs on the MB<sub>4</sub> surface aids in the identification of active areas, the prediction of reactivity, and the optimization of the battery performance. For this purpose, we examined the CDD to envisage the chemical reaction of Ca adsorption on CrB<sub>4</sub>/MoB<sub>4</sub>/WB<sub>4</sub> utilizing the following equation.

$$\Delta\rho(r) = \rho_{\text{Ca-MB}_4}(r) - \rho_{\text{MB}_4}(r) - \rho_{\text{Ca}}(r) \quad (3)$$

In this equation, the charge-density of the MB<sub>4</sub> surface with one Ca atom adsorbed is represented by  $\rho_{\text{Ca-MB}_4}$  and  $\rho_{\text{MB}_4}$  represents the charge-density of pure MB<sub>4</sub> while  $\rho_{\text{Ca}}$  denotes the charge-density of the isolated Ca-atom. As demonstrated in Fig. 3(a–c), while the yellow zone depicts electron accumulation, the green region denotes electron depletion. It shows that a significant amount of charge exchange takes place between the Ca-ion and MB<sub>4</sub> monolayer MBene. There is an extensive charge accumulation between the Ca-atom and MB<sub>4</sub> monolayer MBenes surface, whereas there is charge depletion surrounding the Ca atom. These findings suggest that strong interactions on the surface of MB<sub>4</sub> monolayer MBene may allow Ca ions to be adsorbed steadily.

After finding a suitable adsorption site and the strong interactions with the suitable charge transfer of Ca atom on the MB<sub>4</sub> surface, we examined the possibility of multilayer adsorption in monolayer MB<sub>4</sub> MBenes because the storage capacity of the Ca-ion batteries depends on the number of Ca atoms adsorbed on the surface of MB<sub>4</sub>. We considered the top and bottom hollow site of the monolayer's surface for the further adsorption of Ca-atoms. We adsorbed the triple layers of Ca atoms on both sides, and we adsorbed max 9 Ca-atoms on one layer. In this way, we adsorbed a total of 6 layers on both sides including 3 top and 3 bottom surfaces of MB<sub>4</sub>, and their adsorption scheme is shown in Fig. S11(a–f),<sup>†</sup> which indicates the top side and bottom side view of adsorption of Ca-atoms layer on the surface of CrB<sub>4</sub> from layer 1 to layer 6. The second- and third-layer adsorption involved Ca ions occupying

the T-site site of the first and second layers at different positions of the T-site. The optimized structure of all Ca-layers adsorption on CrB<sub>4</sub>, MoB<sub>4</sub> and WB<sub>4</sub> are shown in Figs. S12–S14(a–f),<sup>†</sup> respectively, which shows that the structure did not significantly change after adsorption, indicating that Ca ion adsorption by triple layers on the top/bottom surface of MB<sub>4</sub> is feasible. The study reveals that MB<sub>4</sub> MBenes can absorb up to six layers (54 atoms) of Ca ions with no alteration in the system's structure and the maximum adsorption contents of Ca atoms are  $x = 6$ , reaching saturation when three layers are adsorbed on each side; we used the following formula to calculate the average adsorption energies ( $E_{\text{ad}}$ ) of Ca-atom layers.<sup>92</sup>

$$E_{\text{ad}} = (E_{\text{MB}_4+x\text{Ca}} - E_{\text{MB}_4} - xE_{\text{Ca}})/x \quad (4)$$

In this instance,  $E_{\text{MB}_4+x\text{Ca}}$  and  $E_{\text{MB}_4}$  represent the total energy of the MB<sub>4</sub> monolayer values with and without Ca-ions adsorption, whereas  $E_{\text{Ca}}$  represents the total energy values of Ca in the bulk phase and “x” is the number of Ca atoms absorbed. The calculated average adsorption energies values of Ca layers on the CrB<sub>4</sub>, MoB<sub>4</sub> and WB<sub>4</sub> monolayer surface are shown in Table 3 and graphically represented in Fig. 2(b). Negative adsorption energy represents the strong interactions between the Ca ions and the MB<sub>4</sub> monolayer. When the number of the adsorption layers increase, the distance between the Ca layers and MB<sub>4</sub> monolayer increases, which is the reason for the weak interactions of the third layer on both sides, but the adsorption energies remain negative, which is favorable, and we cannot add more layer because the adsorption energies become positive. For the adsorption of a single layer of Ca-atom layers, the interaction between the Ca atoms and the substrate is strong, and when we adsorbed the 2nd and 3rd layers, then the interactions became weak and the upper most layer has weak coulombic interactions with the substrate and the adsorption energy decrease. As the number of layers of Ca atoms increased, the coulombic repulsion between the Ca atoms in the intralayer increased owing to the weak interaction with the substrate and

Table 3 Calculated average adsorption energy of the Ca-adsorbed layer on CrB<sub>4</sub>, MoB<sub>4</sub> and WB<sub>4</sub>

Material	$x_1$	$x_2$	$x_3$	$x_4$	$x_5$	$x_6$
CrB <sub>4</sub>	−1.84	−1.36	−0.85	−0.82	−0.36	−0.14
MoB <sub>4</sub>	−1.66	−1.49	−1.01	−0.93	−0.42	−0.11
WB <sub>4</sub>	−1.40	−1.11	−0.62	−0.44	−0.39	−0.27

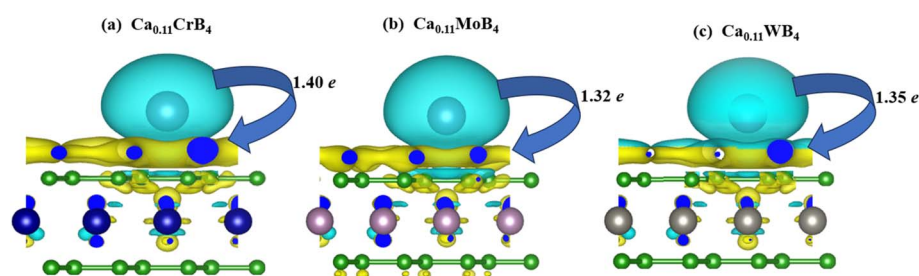


Fig. 3 Charge density difference for the adsorption of single Ca-ion on the substrate (a) CrB<sub>4</sub>, (b) MoB<sub>4</sub>, and (c) WB<sub>4</sub>.

strong coulombic repulsion between Ca atoms. Due to repulsion of Ca atoms in the intralayer, the adsorption energy becomes low but remains negative. Fig. S15† represents the spacing of the interlayer between the adsorbed Ca atoms on the CrB<sub>4</sub>, MoB<sub>4</sub> and WB<sub>4</sub> substrate and it can be seen that with the adsorption of multilayers, the distance from the substrate increases and the largest distance of the last layer with the substrate is 7.95 Å, 7.99 Å and 8.32 Å for CrB<sub>4</sub>, MoB<sub>4</sub> and WB<sub>4</sub>, respectively. The distance of the uppermost layer of the WB<sub>4</sub> layer is larger than CrB<sub>4</sub> and MoB<sub>4</sub> due to the larger atomic size of tungsten atom as compared to Cr and Mo, which shows the strong interactions of Ca atom on the surface of CrB<sub>4</sub> as compared to that of MoB<sub>4</sub> and WB<sub>4</sub>. The concentration of Ca ions adsorbed on CrB<sub>4</sub>/MoB<sub>4</sub>/WB<sub>4</sub> reaches its maximum when the attracting and repulsive electrostatic forces between the Ca ions completely balance each other out. Thus, we cannot consider additional metal layers adsorbed onto the substrate.

The formation of a negative electron cloud (NEC) is important for the structural stability of the materials with adsorption and helps to further attract the outer-ions when examining the layer-by-layer adsorption of Ca ions. The valence electron localization function (ELF) is an effective method for analyzing the interactions between Ca ions and the adsorption layer and substrate. In order to illustrate the adsorption mechanism of various Ca ions, we determined the ELF of the (1 0 0) section for the maximum layers of Ca adsorbed on the MB<sub>4</sub> monolayer, as illustrated in Fig. 4(a–c). It should be noted that an electron's full localization is represented by an ELF value of 1, and that the electron-gas-like pair probability is represented by a value of 0.5; the lower value denotes a lower electron density.<sup>93</sup> Ionic bond formation was evident in Fig. 4 as electrons were localized between the MB<sub>4</sub> substrate and the first layer Ca atoms. This demonstrates that the initial layer's steady adsorption of each of these metals is confirmed. Additionally, an integrated NEC layer forms over the Ca layer, guaranteeing the first-layer Ca ions' persistent adsorption on the MB<sub>4</sub> surface and increasing the attraction of additional Ca ions. The localization between the outmost adsorbed Ca atoms steadily rises with the increasing number of adsorption Ca layers. The existence of NEC between Ca layers significantly reduces atom-to-atom repulsion and is

essential for enhancing the stability of multilayer adsorption. These findings demonstrate how the covalent and ionic bonds within the MB<sub>4</sub> monolayer coexist, which enhances the monolayer's exceptional structural stability. The Ca ions were almost entirely ionized in each case, suggesting a substantial chemical interaction between these Ca ions and the MB<sub>4</sub> monolayer. By fostering the formation of both covalent and ionic interactions, this robust interaction supports the general stability and adsorption behavior of Ca on the outer MB<sub>4</sub> layer.

To check the thermodynamic stability of the structures, we calculated the formation energy using the following equation.<sup>94</sup>

$$E_f = (E_{\text{MB}_4+x\text{Ca}} - E_{\text{MB}_4} - xE_{\text{Ca}})/x + 1 \quad (5)$$

In this case,  $E_{\text{MB}_4+x\text{Ca}}$  and  $E_{\text{MB}_4}$  represent the total energy of the MB<sub>4</sub> monolayer values with and without Ca ions adsorption, whereas  $E_{\text{Ca}}$  represents the total energy values of Ca in the bulk phase and “ $x$ ” is the number of Ca atoms absorbed. The formation energies and the constructed convex hull of Ca-adsorbed MB<sub>4</sub> (M = Cr, Mo, and W) at different concentrations are displayed in Fig. S16(a–c).† For MB<sub>4</sub> structures with Ca adsorbed, we computed six concentrations. Convex hulls form solid lines connecting minimal energies, making thermodynamically stable states. MB<sub>4</sub> monolayer's stable structure and less volume fluctuations benefit its cycle stability and performance as an anode in CIBs for Ca-ion insertion and extraction sequences. Notably, Ca adsorbed-MB<sub>4</sub>'s  $E_f$  curves ( $x = 1, 2, 3, 4, 5,$  and  $6$ ) show stability, like the earlier studied two-dimensional materials.<sup>95–97</sup>

### 3.3 Thermal stability

Thermal stability is crucial in calcium-ion batteries to prevent structure deformation, which can compromise the battery's integrity and performance. It prevents excessive expansion or contraction, preserving the structural integrity during the charge and discharge cycles. This prevents mechanical stresses like electrode cracking, particle detachment, or electrolyte leakage, ensuring reliable and long-lasting performance in various operating conditions.

The thermal stability of MB<sub>4</sub> monolayers with Ca ions at various concentrations was investigated using an *ab initio* molecular dynamics (AIMD) method under the NVT ensemble, and we considered the pristine as well as Ca-ion adsorbed monolayer of MB<sub>4</sub> for a  $3 \times 3 \times 1$  supercell. Fig. S17(a–c)† correspond to the energy changes with time steps for the pristine CrB<sub>4</sub>, MoB<sub>4</sub>, and WB<sub>4</sub> monolayer, respectively, and shows the zero structural deformation of the pure material. From Fig. S18(a–c),† the simulation resulted in the preservation of the two layers of Ca-adsorbed MB<sub>4</sub> monolayer's structural integrity, as evidenced by the simulation's modest oscillations that suggested the monolayer's stability. Nonetheless, the system's energy did not significantly change over the course of the simulation. The structures of Ca<sub>2</sub>CrB<sub>4</sub>, Ca<sub>2</sub>MoB<sub>4</sub>, and Ca<sub>2</sub>WB<sub>4</sub> did not undergo any notable alterations or deformations during the Ca adsorption process, as demonstrated by our simulated timeline spanning from 1 to 5000 fs. Fig. S19(a–c)† represent the molecular dynamic simulations of full concentrations of Ca

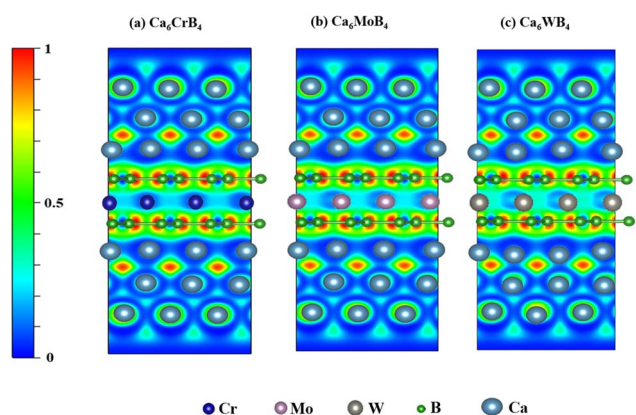


Fig. 4 Electron localization functions (ELFs) of the (100) section on (a) Ca<sub>6</sub>CrB<sub>4</sub>, (b) Ca<sub>6</sub>MoB<sub>4</sub>, and (c) Ca<sub>6</sub>WB<sub>4</sub>.

ions adsorbed on  $\text{CrB}_4$ ,  $\text{MoB}_4$  and  $\text{WB}_4$  at 300 K, and we can see that the small structural disorder occurs, which is acceptable according to the literature.<sup>98–102</sup> Additionally, in order to validate the  $\text{MB}_4$  ( $M = \text{Cr}, \text{Mo}, \text{W}$ ) monolayer's thermal stability at high temperatures, we also ran simulations on its maximum Ca configurations at 500 K. The results indicated that the small structures are disordered just like those at 300 K, confirming their stability at high temperatures, as shown in Fig. S20(a–c).† The atomic recombination and chemically breaking of bonds are almost invisible, which is in keeping with the previously reported 2D materials.<sup>98–102</sup> Remarkably, during the adsorption/desorption process, the volume of the Ca ions-adsorbed  $\text{MB}_4$  MBenes was less changed than graphite.<sup>103,104</sup> Our findings also showed low energy fluctuations, which supports the thermal and dynamic stability of  $\text{MB}_4$  at room temperature.

### 3.4 Diffusion barrier

To better understand the correlation between the rate capability and cyclability of batteries and the diffusion behavior of Ca ions on the electrode surface, we investigated the diffusion properties of Ca ions on  $\text{MB}_4$  ( $M = \text{Cr}, \text{Mo}, \text{W}$ ) monolayer. The energy barrier for Ca ion diffusion for the  $\text{MB}_4$  monolayer was examined using the CI-NEB method. The energy barrier represents the energy required for the diffusion process to occur. Additionally, we calculated the Ca atoms'  $\text{MB}_4$  diffusion coefficient

( $D$ ) as a function of temperature using the Arrhenius equation as  $D(T) = a^2\nu_0e^{-E_b/k_B T}$ .<sup>105</sup> Here,  $\nu_0$  is the vibrational frequency ( $10^{13}$  Hz),  $E_b$  is the diffusion barrier, and “ $a$ ” is the Ca-atom movement distance within the  $\text{MB}_4$  monolayer at the adsorption sites. Absolute temperature and Boltzmann constant are represented by the symbols  $T$  and  $k_B$ , respectively. The diffusion barrier in Ca-ion batteries controls the movement of Ca ions between the  $\text{MB}_4$  materials that make up the battery electrode. Diffusion barriers are used in charging and discharging processes to regulate the speed at which ions may move through a substance. Essentially, the lower the energy barrier, the faster the process of ion diffusion. So, by finding the pathway with the lowest diffusion barrier, we can understand the structural symmetry to find the best diffusion path. Considering that Ca tends to be adsorbed on site H1, the possible migration path according to the symmetry of our structure is shown in Fig. 5(a). We considered the two paths as path-1 (H1–H2) starting from the H1-site to the H2-site, and path-2 (H1–T–H2) starting from the H1-site to the H2-site through the T-site.

To illustrate the process of diffusion and how it progresses between the initial and final site, we chose the three intermediate images, and these images give extra clarification about the diffusion process. Using these intermediate-stage images, we can see the diffusion process from start to end and examine the energy barriers at every turn. The calculated results and

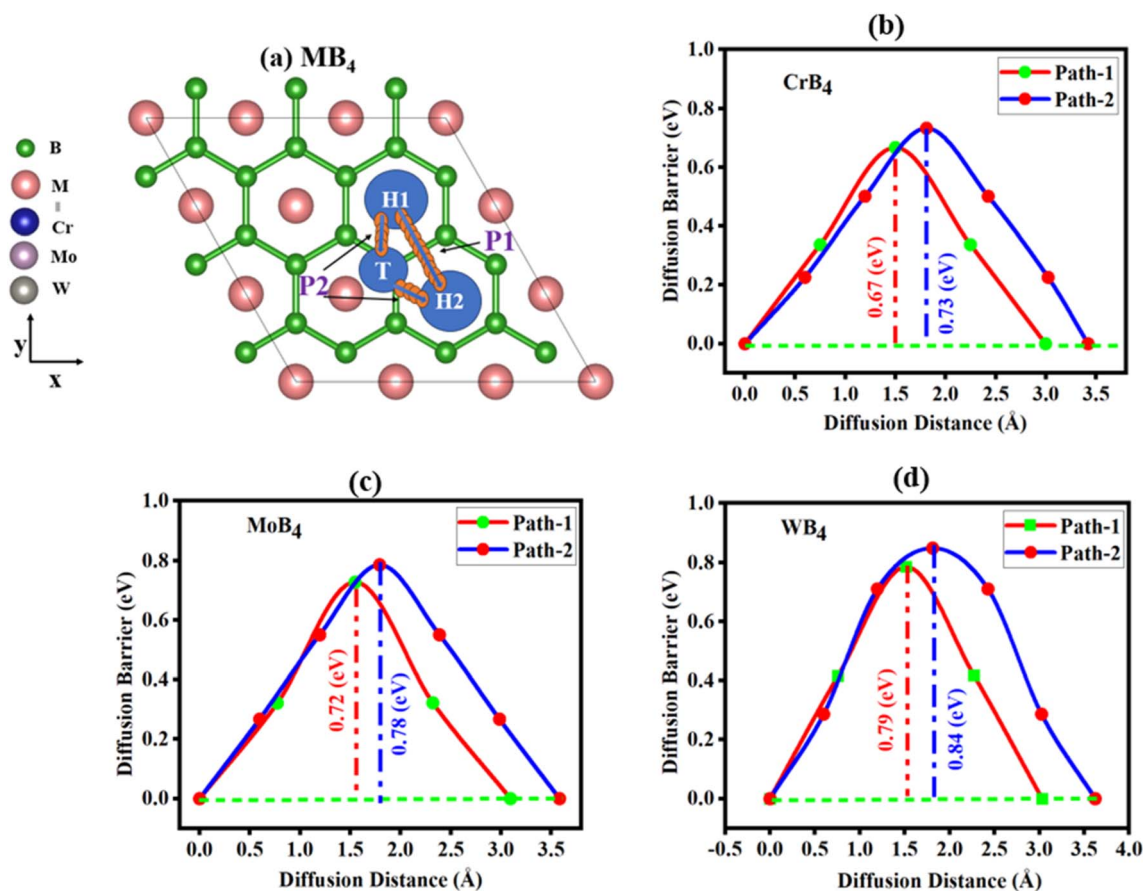


Fig. 5 (a) Migration path 1 (H1–H2) and path 2 (H1–T–H2) for Ca-ions on the  $\text{MB}_4$  monolayer, diffusion energy barriers for Ca-ion diffusion on (b)  $\text{CrB}_4$ , (c)  $\text{MoB}_4$ , and (d)  $\text{WB}_4$ .

schematic diagrams of Ca diffusing on the MB<sub>4</sub> monolayer are summarized in Fig. 5(b–d). The energy barrier profiles show that path-1 has the energy barriers of 0.67 eV, 0.72 eV and 0.79 eV, while path-2 has 0.73 eV, 0.78 eV and 0.84 eV for CrB<sub>4</sub>, MoB<sub>4</sub> and WB<sub>4</sub>, respectively. In comparison to CrB<sub>4</sub> and MoB<sub>4</sub>, the WB<sub>4</sub> surface exhibits high diffusion barriers. This is likely due to the fact that W contains a larger atomic size than Cr and Mo, which could impact Ca-ion interaction with the lattice and raise the diffusion barrier. The results indicate that path-1 has a lower energy barrier than path-2. Our calculated energy barriers are less than the other materials reported for multivalent ion batteries such as  $\alpha$ -V<sub>2</sub>O<sub>5</sub> (1.63),<sup>106</sup>  $\alpha$ -SN (1.58 eV),<sup>107</sup> FePS<sub>3</sub> (1.18),<sup>108</sup> 2D boron (0.79 eV),<sup>109</sup> TiO<sub>2</sub> (1.27 eV),<sup>110</sup> MoS<sub>2</sub> (1.12 eV)<sup>111</sup> and  $\alpha$ -SN (1.58 eV).<sup>107</sup> Moreover, these values are greater than some reported 2D anode materials such as borophene (0.62 eV),<sup>112</sup> C<sub>2</sub>N (0.30),<sup>113</sup> h-BN (0.10 eV),<sup>114</sup> bismuthine (0.15 eV),<sup>115</sup> and borophene (0.35 eV).<sup>116</sup> Moreover, the comparison with other reported 2D materials is tabulated in Table 4 and graphically represented in Fig. S21.† Ca atoms can diffuse over the surface of monolayers CrB<sub>4</sub>, MoB<sub>4</sub>, and WB<sub>4</sub> with low diffusion potential barriers that allow for quick Ca-ion movement, which boosts the energy efficiency, improves 1.12 cycle stability, and optimizes 1.12 electrochemical performance, preventing undesirable side reactions, guaranteeing the battery's lifespan, and raising the battery's overall efficiency and energy density. All these features make the CrB<sub>4</sub>, MoB<sub>4</sub>, and WB<sub>4</sub> monolayer excellent anode materials for calcium ion batteries.

In practical terms, the adsorption of Ca ions is known to cause considerable volume expansion in electrode materials, hence shortening their service life. Additionally, volume modification is a critical parameter that is examined throughout the monolayer's calcification/decalcification process. For the purpose of volume expansions, the lattice mismatch between the Ca-ions layers and the MB<sub>4</sub> substrate is crucial to the adsorption process, and the smaller the lattice mismatch, the

stronger the adsorption of the higher layers.<sup>120,121</sup> When the Ca content increases, we compute the lattice mismatch as shown in Fig. S22(a–c),† which represents the lattice parameters of Ca<sub>x</sub>MB<sub>4</sub> with increasing Ca contents. The findings show that the lattice constants change as Ca concentrations rise and at maximal Ca content loading, a very slight lattice mismatch was found. The lattice mismatch values for CrB<sub>4</sub>, MoB<sub>4</sub> and WB<sub>4</sub> at  $x = 6$  are 5.94%, 6.16% and 6.31%, respectively. These results validate that there is no cause for concern over lattice mismatch and the adsorption is feasible.

### 3.5 Electrochemical attributes of Ca-adsorbed MB<sub>4</sub>

Ca ions are continuously intercalated into the anode and deintercalated from the cathode in the rocking chair battery during the procedure of charging. The amount of Ca ions that anode materials can store establishes the battery's capacity and it is the number of Ca ions storable per unit mass, which is very important for an efficient electrode material, and the theoretical specific capacity calculation should be based on the structure's maximum Ca intercalation. According to the structure symmetry, we adsorbed Ca atoms on the top/bottom hollow site, 3 layers on the top and three layers on the bottom side with total 54 atoms (9 atoms per layer). The calculated theoretical capacities are 3377 mA h g<sup>-1</sup>, 2311 mA h g<sup>-1</sup> and 1416 mA h g<sup>-1</sup> for CrB<sub>4</sub>, MoB<sub>4</sub> and WB<sub>4</sub>, respectively, for calcium ion batteries. Our calculated values are higher those of commercially available anode materials like SW-BN (1162.66 mA h g<sup>-1</sup>),<sup>117</sup> graphite (284 mA h g<sup>-1</sup>),<sup>91</sup> MoO<sub>2</sub> (1256 mA h g<sup>-1</sup>),<sup>122</sup> Ti<sub>3</sub>C<sub>2</sub> (352 mA h g<sup>-1</sup>),<sup>90</sup> Mo<sub>2</sub>C (560 mA h g<sup>-1</sup>),<sup>123</sup> BC<sub>2</sub>N (840 mA h g<sup>-1</sup>),<sup>124</sup> and super-B (3718 mA h g<sup>-1</sup>),<sup>125</sup> and the comparison with other reported 2D materials is tabulated in Table 4 and graphically represented in Fig. S21.† Within the saturation concentration range, the theoretical storage capacity rises significantly, boasting approximately five times the capacity of graphite, a typical anode material for LIBs.

Subsequently, the average open-circuit voltages associated with the amounts of several Ca cations that are adsorbed were computed. When charging and discharging, the electron potential energy process equals the variation in Gibbs free energy inside the system. The change in the total energy of the Ca atoms before and after adsorption is about equal to this change in the Gibbs free energy when we ignore the small changes in the system's volume and entropy. The open circuit voltage is mostly influenced by the Ca ion distribution in the system, which is defined by the energy differential between two systems with various concentrations of adsorption. To do this, we applied varying concentrations of Ca ions to both sides of the monolayer MB<sub>4</sub> MBenes until they were fully covered, using the Ca<sub>x</sub>MB<sub>4</sub> stoichiometry ( $x = 1, 2, 3, 4, 5, 6$ ). After numerical stabilization in Fig. 6, we used the average voltage curves to calculate the average open-circuit voltages, which shows the decreasing trends of the voltage as the number of Ca layers increased. Our calculated average OCV values are 0.45 V, 0.47 V and 0.35 V for Ca<sub>x</sub>CrB<sub>4</sub>, Ca<sub>x</sub>MoB<sub>4</sub> and Ca<sub>x</sub>WB<sub>4</sub>, which are lower than that for phosphorene (0.83 V),<sup>126</sup> TiO<sub>2</sub> (1.5 V)<sup>127</sup> and borophene (2.63 V).<sup>112</sup> The comparison with other reported 2D

**Table 4** Comparison of voltage, diffusion barrier, and capacity of MB<sub>4</sub> with those of other materials

Material	Voltage (V)	Diffusion barrier (eV)	Capacity (mA h g <sup>-1</sup> )	Ref.
CrB <sub>4</sub>	0.45	0.67	3377	This work
MoB <sub>4</sub>	0.47	0.72	2311	This work
WB <sub>4</sub>	0.35	0.79	1416	This work
SrB <sub>8</sub>	0.48	0.67	616	47
Borophene	1.59	0.62	964	112
2D boron	1.50	0.79	2125	109
SW-BN	0.89	0.11	1162	117
C <sub>2</sub> N	0.23	0.30	419	113
FePS <sub>3</sub>	0.48	1.18	586	108
TiS <sub>2</sub>	1.4	1.16	—	118
BSi	0.40	1.08	2749	119
C <sub>2</sub> N	0.23	0.30	419	113
FePS <sub>3</sub>	0.48	1.18	586	108

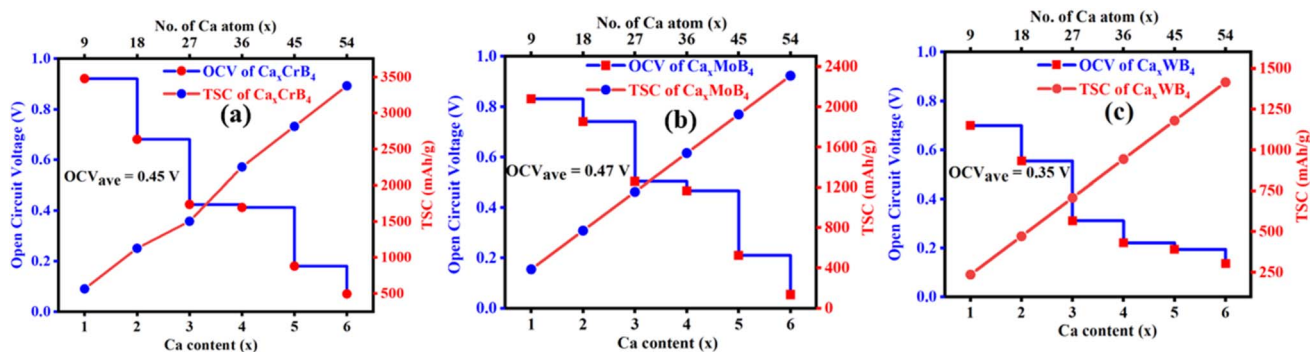


Fig. 6 Theoretical storage capacity (TSC) and average open circuit voltage (OCV) of (a)  $\text{Ca}_x\text{CrB}_4$ , (b)  $\text{Ca}_x\text{MoB}_4$ , and (c)  $\text{Ca}_x\text{WB}_4$ .

materials is tabulated in Table 4. It is significant that these average OCV values are within the recommended range of 0–1.0 V for anode materials that are readily available for use in metal ion batteries.<sup>128</sup>

### 3.6 Electronic structure and conductivity

A desirable anode material's high electronic conductivity is a feature that directly impacts the battery's performance. A battery's internal electronic resistance is mostly determined by

its electronic conductivity. The electronic structure of the  $\text{MB}_4$  ( $M = \text{Cr}, \text{Mo}, \text{and W}$ ) monolayer was investigated using GGA-PBE calculations. Fig. S23(a–c)† reveal that the pristine monolayers are metallic in nature. Band structures show the two Dirac cones, one is located over the Fermi level and the other is located just below the Fermi level. These cones have velocity nearly equal to that of graphene. Some energy bands cross the Fermi level and show the metallic conductivity, which is the best for Ca-ion batteries. Fig. 7(a–c) represent the total density

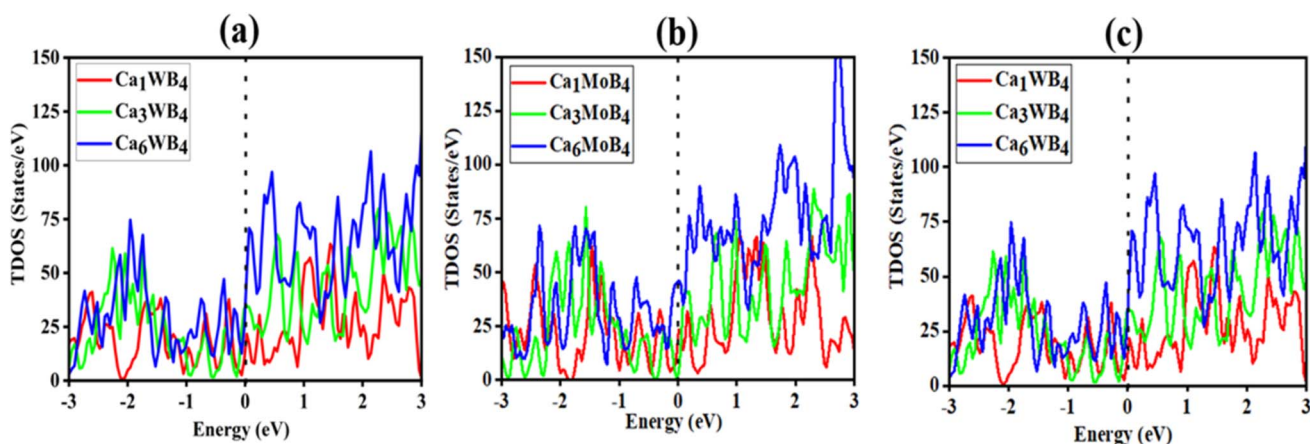


Fig. 7 Total density of states of Ca adsorption for different contents of (a)  $\text{Ca}_x\text{CrB}_4$ , (b)  $\text{Ca}_x\text{MoB}_4$ , and (c)  $\text{Ca}_x\text{WB}_4$ .

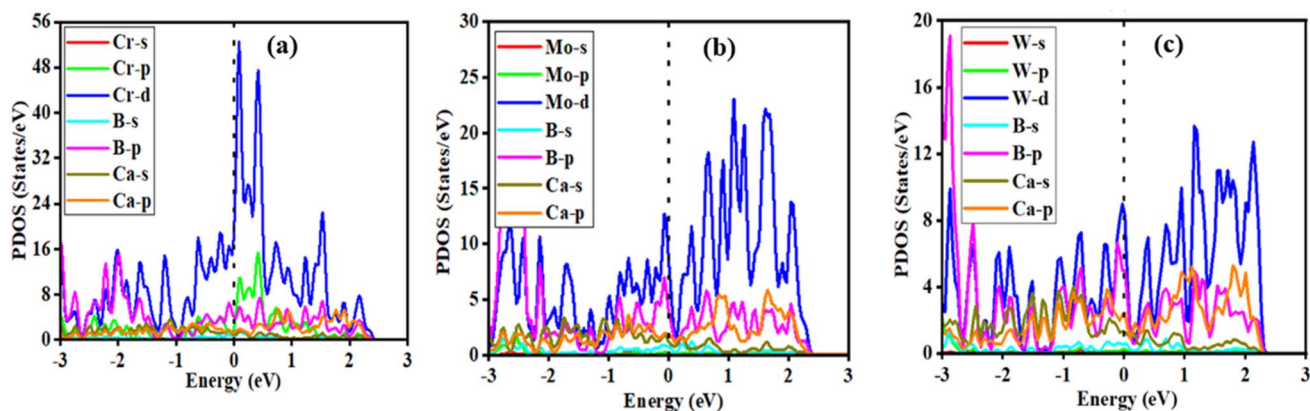


Fig. 8 PDOS of the highest contents of Ca in (a)  $\text{Ca}_6\text{CrB}_4$ , (b)  $\text{Ca}_6\text{MoB}_4$ , and (c)  $\text{Ca}_6\text{WB}_4$ .

of state for one, three and six layers-adsorbed MB<sub>4</sub>. It can be shown that when we increase the number of layers of the Ca atom, then the number of electronic states also increase at the Fermi level, which indicates the more accessible active electrons in the system. Fig. S23<sup>†</sup> represents the PDOS of pristine CrB<sub>4</sub>, MoB<sub>4</sub> and WB<sub>4</sub>, which show the main contribution of the d-state of Cr/Mo/W atom and the p-state of the B-atom and after the adsorption of full contents (6 layers) of Ca atoms; we can see from Fig. 8(d–f) that the main contribution is also due to the d-state of Cr/Mo/W atom and the p-state of the B-atom of the CrB<sub>4</sub>, MoB<sub>4</sub> and WB<sub>4</sub> host materials. For the Ca atom, only the p-state is dominant as compared to the s-state for the CrB<sub>4</sub>, MoB<sub>4</sub> and WB<sub>4</sub> host materials. Other states indirectly contribute to the electrical conductivity, but their influence is minimal compared to these states. It can be seen that after the adsorption of the Ca-atoms layers, the metallic nature of the materials remains the same and the electrical conductivity of the material is increased. It is observed that the charge carrier transfer to the conduction band results in an increase in the electronic conductivity, suggesting that all materials have the capacity to serve as appropriate hosts for Ca-ion batteries.

## 4 Conclusions

Density functional theory calculations have been used to predict the performance of CrB<sub>4</sub>, MoB<sub>4</sub> and WB<sub>4</sub> monolayers as anode materials for calcium ion batteries. The results shows that the electrical conductivity is enhanced, while the metallicity remains unchanged. After the adsorption of Ca atoms, the adsorption energy is steadily reduced as the quantity of adsorbed Ca ions increased. The average open circuit voltage and energy barriers are 0.45 V, 0.67 eV for CrB<sub>4</sub>, 0.47 V and 0.72 eV for MoB<sub>4</sub>, and 0.35 V and 0.79 eV for WB<sub>4</sub>. For the most stable site, Ca atom transferred a charge of 1.40e to the monolayer CrB<sub>4</sub>, 1.32e to the monolayer MoB<sub>4</sub> and 1.35e to the monolayer WB<sub>4</sub>. The largest distance of the last layer to the substrate is 7.95 Å, 7.99 Å and 8.32 Å for CrB<sub>4</sub>, MoB<sub>4</sub> and WB<sub>4</sub>, respectively. ELF findings demonstrate how the covalent and ionic bonds within the MB<sub>4</sub> monolayer coexist, which enhances the monolayer's exceptional structural stability. The volume expansion values for CrB<sub>4</sub>, MoB<sub>4</sub> and WB<sub>4</sub> at x = 6 are 5.94%, 6.16% and 6.31%, respectively. The calculated theoretical capacities are 3377 mA h g<sup>-1</sup>, 2311 mA h g<sup>-1</sup> and 1416 mA h g<sup>-1</sup>, and the energy barrier profiles show that path-1 has the lowest energy barriers of 0.67 eV, 0.72 eV and 0.79 eV for CrB<sub>4</sub>, MoB<sub>4</sub> and WB<sub>4</sub>. In conclusion, the monolayers of CrB<sub>4</sub>, MoB<sub>4</sub> and WB<sub>4</sub> offer several advantages, including excellent stability, low diffusion barriers, and a high theoretical capacity. These materials show promise as anode materials for Ca-ion batteries and may find practical applications in future commercial battery materials. Our research aims to provide essential insights into the feasibility of incorporating monolayer MB<sub>4</sub> in Ca-ion battery technology.

## Data availability

Data supporting the findings of this study are available in the ESI<sup>†</sup> accompanying this article. Additional data that support the

findings of this study are available from the corresponding author upon reasonable request.

## Author contributions

M. Kashif Masood: visualization, methodology, formal analysis, writing – original draft investigation. Jing Wang: revision, formal analysis, discussion, conceptualization, and acquisition for funding. Juntao Song: project administration, resources, visualization, supervision. Ying Liu: conceptualization, visualization, formal analysis and resources.

## Conflicts of interest

Authors have no conflicts of interest to declare.

## Acknowledgements

This research is funded by The National Natural Science Foundation of China (Grant No. 12174084), Science Research Project of Hebei Education Department (Grant No. ZD2021065), and The Key Program of Natural Science Foundation of Hebei Province (Grant No. A2021205024).

## References

- 1 F. N. U. Khan, *et al.*, Design and optimization of lithium-ion battery as an efficient energy storage device for electric vehicles: A comprehensive review, *J. Energy Storage*, 2023, **71**, 108033.
- 2 S. Ahmed, *et al.*, First Principles Study of Layered CrGeTe<sub>3</sub> as Lithium Intercalation Compound, *J. Electrochem. Soc.*, 2022, **169**(4), 040557.
- 3 N. Yabuuchi, *et al.*, Research development on sodium-ion batteries, *Chem. Rev.*, 2014, **114**(23), 11636–11682.
- 4 M. I. Khan, *et al.*, Intercalation of Lithium inside bilayer buckled borophene: a first principles prospective, *J. Electrochem. Soc.*, 2021, **168**(7), 070535.
- 5 M. K. Masood, *et al.*, A novel two-dimensional monolayer MB<sub>4</sub> (M= Cr, Mo, W) MBenes as a high-performance anode material for Mg-ion batteries, *J. Energy Storage*, 2024, **86**, 111370.
- 6 P. Kulkarni, *et al.*, A comprehensive review of pre-lithiation/sodiation additives for Li-ion and Na-ion batteries, *J. Energy Chem.*, 2023, **76**, 479–494.
- 7 J. Hu, *et al.*, Emerging organic electrodes for Na-ion and K-ion batteries, *Energy Storage Mater.*, 2023, **56**, 267–299.
- 8 H. Tang, *et al.*, Magnesium ion-doped layered oxide cathodes for alkali-metal ion batteries: recent research progress and outlook, *Energy Storage Mater.*, 2023, 102935.
- 9 R. Zhou, *et al.*, An advanced organic cathode for non-aqueous and aqueous calcium-based dual ion batteries, *J. Power Sources*, 2023, **569**, 232995.
- 10 Q. Ran, *et al.*, Uniformly MXene-Grafted Eutectic Aluminum-Cerium Alloys as Flexible and Reversible Anode Materials for Rechargeable Aluminum-Ion Battery, *Adv. Funct. Mater.*, 2023, **33**(1), 2211271.

- 11 X. Xiang, K. Zhang and J. Chen, Recent advances and prospects of cathode materials for sodium-ion batteries, *Adv. Mater.*, 2015, **27**(36), 5343–5364.
- 12 S. W. Kim, *et al.*, Electrode materials for rechargeable sodium-ion batteries: potential alternatives to current lithium-ion batteries, *Adv. Energy Mater.*, 2012, **2**(7), 710–721.
- 13 M. I. Khan, *et al.*, Computational insights of alkali metal (Li/Na/K) atom decorated buckled bismuthene for hydrogen storage, *Int. J. Hydrogen Energy*, 2021, **46**(56), 28700–28708.
- 14 M. Mohammadi and G. R. Vakili-Nezhaad, First-Principles Calculations of Graphene-WS<sub>2</sub> Nanoribbons As Electrode Material for Magnesium-Ion Batteries, *J. Electron. Mater.*, 2022, 1–7.
- 15 L. Wang, *et al.*, High-Rate and Long Cycle-Life Alloy-Type Magnesium-Ion Battery Anode Enabled Through (De) magnesiation-Induced Near-Room-Temperature Solid–Liquid Phase Transformation, *Adv. Energy Mater.*, 2019, **9**(45), 1902086.
- 16 Y. Cheng, *et al.*, Interface promoted reversible Mg insertion in nanostructured Tin–Antimony Alloys, *Adv. Mater.*, 2015, **27**(42), 6598–6605.
- 17 H. Zhang, *et al.*, High mobility and high storage capacity of lithium in sp–sp<sup>2</sup> hybridized carbon network: the case of graphyne, *J. Phys. Chem. C*, 2011, **115**(17), 8845–8850.
- 18 P. Ganesh, *et al.*, Binding and diffusion of lithium in graphite: quantum monte carlo benchmarks and validation of van der Waals density functional methods, *J. Chem. Theory Comput.*, 2014, **10**(12), 5318–5323.
- 19 E. Pomerantseva and Y. Gogotsi, Two-dimensional heterostructures for energy storage, *Nat. Energy*, 2017, **2**(7), 1–6.
- 20 H. Wang, *et al.*, Siligraphene as a promising anode material for lithium-ion batteries predicted from first-principles calculations, *Nano Energy*, 2018, **49**, 67–76.
- 21 Q. Kong, *et al.*, SiS nanosheets as a promising anode material for Li-ion batteries: a computational study, *Phys. Chem. Chem. Phys.*, 2017, **19**(12), 8563–8567.
- 22 D. Das, *et al.*, Monolayer BC<sub>2</sub>: an ultrahigh capacity anode material for Li ion batteries, *Phys. Chem. Chem. Phys.*, 2017, **19**(35), 24230–24239.
- 23 A. Gupta, T. Sakthivel and S. Seal, Recent development in 2D materials beyond graphene, *Prog. Mater. Sci.*, 2015, **73**, 44–126.
- 24 M. Liang and L. Zhi, Graphene-based electrode materials for rechargeable lithium batteries, *J. Mater. Chem.*, 2009, **19**(33), 5871–5878.
- 25 G. Kucinskis, G. Bajars and J. Kleperis, Graphene in lithium ion battery cathode materials: A review, *J. Power Sources*, 2013, **240**, 66–79.
- 26 G. A. Tritsarlis, *et al.*, Adsorption and diffusion of lithium on layered silicon for Li-ion storage, *Nano Lett.*, 2013, **13**(5), 2258–2263.
- 27 R. Zhang, X. Wu and J. Yang, Blockage of ultrafast and directional diffusion of Li atoms on phosphorene with intrinsic defects, *Nanoscale*, 2016, **8**(7), 4001–4006.
- 28 V. V. Kulish, *et al.*, Phosphorene as an anode material for Na-ion batteries: a first-principles study, *Phys. Chem. Chem. Phys.*, 2015, **17**(21), 13921–13928.
- 29 P. Liang, *et al.*, Is borophene a suitable anode material for sodium ion battery?, *J. Alloys Compd.*, 2017, **704**, 152–159.
- 30 H. Jiang, *et al.*, Borophene: a promising anode material offering high specific capacity and high rate capability for lithium-ion batteries, *Nano Energy*, 2016, **23**, 97–104.
- 31 H. Jiang, *et al.*, Boron phosphide monolayer as a potential anode material for alkali metal-based batteries, *J. Mater. Chem. A*, 2017, **5**(2), 672–679.
- 32 Q. Sun, *et al.*, Ab initio prediction and characterization of Mo<sub>2</sub>C monolayer as anodes for lithium-ion and sodium-ion batteries, *J. Phys. Chem. Lett.*, 2016, **7**(6), 937–943.
- 33 M. Naguib, *et al.*, Two-dimensional transition metal carbides, *ACS Nano*, 2012, **6**(2), 1322–1331.
- 34 M. Naguib, *et al.*, Two-dimensional nanocrystals produced by exfoliation of Ti<sub>3</sub>AlC<sub>2</sub>, in *MXenes*, Jenny Stanford Publishing, 2011, pp. 15–29.
- 35 Z. Guo, J. Zhou and Z. Sun, New two-dimensional transition metal borides for Li ion batteries and electrocatalysis, *J. Mater. Chem. A*, 2017, **5**(45), 23530–23535.
- 36 Z. Jiang, *et al.*, MBene (MnB): a new type of 2D metallic ferromagnet with high Curie temperature, *Nanoscale Horiz.*, 2018, **3**(3), 335–341.
- 37 T. Yu, *et al.*, TiC<sub>3</sub> monolayer with high specific capacity for sodium-ion batteries, *J. Am. Chem. Soc.*, 2018, **140**(18), 5962–5968.
- 38 D. Fan, *et al.*, Two-dimensional tetragonal titanium carbide: A high-capacity and high-rate battery material, *J. Phys. Chem. C*, 2018, **122**(27), 15118–15124.
- 39 J. Jia, *et al.*, Monolayer MBenes: prediction of anode materials for high-performance lithium/sodium ion batteries, *Nanoscale*, 2019, **11**(42), 20307–20314.
- 40 H. Zhang, *et al.*, First demonstration of possible two-dimensional MBene CrB derived from MAB phase Cr<sub>2</sub>AlB<sub>2</sub>, *J. Mater. Sci. Technol.*, 2018, **34**(11), 2022–2026.
- 41 L. T. Alameda, *et al.*, Topochemical deintercalation of Al from MoAlB: stepwise etching pathway, layered intergrowth structures, and two-dimensional MBene, *J. Am. Chem. Soc.*, 2018, **140**(28), 8833–8840.
- 42 S. Anantharaj, *et al.*, Recent trends and perspectives in electrochemical water splitting with an emphasis on sulfide, selenide, and phosphide catalysts of Fe, Co, and Ni: a review, *ACS Catal.*, 2016, **6**(12), 8069–8097.
- 43 Y. Lin, *et al.*, Designed borophene/TMDs hybrid catalysts for enhanced hydrogen evolution reactions, *J. Mater. Chem. C*, 2021, **9**(44), 15877–15885.
- 44 A. VahidMohammadi, J. Rosen and Y. Gogotsi, The world of two-dimensional carbides and nitrides (MXenes), *Science*, 2021, **372**(6547), eabf1581.
- 45 M.-R. Gao, *et al.*, Nanostructured metal chalcogenides: synthesis, modification, and applications in energy conversion and storage devices, *Chem. Soc. Rev.*, 2013, **42**(7), 2986–3017.
- 46 V. G. Nair, *et al.*, 2D MBenes: A novel member in the flatland, *Adv. Mater.*, 2022, **34**(23), 2108840.

- 47 Y. Wang, *et al.*, TiB 4 and SrB 8 monolayers: high capacity and zero strain-like anode materials for Li/Na/K/Ca ion batteries, *Phys. Chem. Chem. Phys.*, 2024, **26**(5), 4455–4465.
- 48 Y. Wang, *et al.*, On two-dimensional metal borides (MBenes) as anode materials for metal-ion batteries: A first-principles study, *Comput. Mater. Sci.*, 2024, **233**, 112710.
- 49 Y. Li, *et al.*, Computational evaluation of ScB and TiB MBenes as promising anode materials for high-performance metal-ion batteries, *Phys. Rev. Mater.*, 2022, **6**(4), 045801.
- 50 D. Wang, *et al.*, First-principles calculations of Ti<sub>2</sub>N and Ti<sub>2</sub>NT<sub>2</sub> (T= O, F, OH) monolayers as potential anode materials for lithium-ion batteries and beyond, *J. Phys. Chem. C*, 2017, **121**(24), 13025–13034.
- 51 (a) M. Naguib, *et al.*, *ACS Nano*, 2012, **6**, 1322; (b) Y. Xie, Y. Dall'Agnese, M. Naguib, Y. Gogotsi, M. W. Barsoum, H. L. Zhuang and P. R. Kent, *ACS Nano*, 2014, **8**, 9606.
- 52 Y. Li, *et al.*, Computational determination of a graphene-like TiB 4 monolayer for metal-ion batteries and a nitrogen reduction electrocatalyst, *Phys. Chem. Chem. Phys.*, 2023, **25**(10), 7436–7444.
- 53 N. Ma, *et al.*, New phases of MBenes M<sub>2</sub>B (M= Sc, Ti, and V) as high-capacity electrode materials for rechargeable magnesium ion batteries, *Appl. Surf. Sci.*, 2022, **571**, 151275.
- 54 G. Kresse and J. Furthmüller, *Phys. Rev. B: Condens. Matter Mater. Phys.*, 1996, **55**(12), 7539.
- 55 G. Kresse and D. Joubert, From ultrasoft pseudopotentials to the projector augmented-wave method, *Phys. Rev. B: Condens. Matter Mater. Phys.*, 1999, **59**(3), 1758.
- 56 M. Benhamida, N. Baadji and K. Bouamama, Computational Study of Mechanical and Electronic Properties of Transition Metal Carbides Ti<sub>x</sub>M<sub>1-x</sub>C with M= Nb, V and Zr, *J. Nanoelectron. Optoelectron.*, 2019, **14**(5), 622–625.
- 57 J. Perdew and Y. Wang, *Phys. Rev. B: Condens. Matter Mater. Phys.*, 1986, 8822–8824.
- 58 J. Nisar, *et al.*, Optical gap and native point defects in kaolinite studied by the GGA-PBE, HSE functional, and GW approaches, *Phys. Rev. B: Condens. Matter Mater. Phys.*, 2011, **84**(7), 075120.
- 59 R. Pela, M. Marques and L. Teles, Comparing LDA-1/2, HSE03, HSE06 and G0W0 approaches for band gap calculations of alloys, *J. Phys.: Condens. Matter*, 2015, **27**(50), 505502.
- 60 Y.-S. Lin, *et al.*, Long-range corrected hybrid density functionals with improved dispersion corrections, *J. Chem. Theory Comput.*, 2013, **9**(1), 263–272.
- 61 S. Kumari, *et al.*, Synergistic plasma-assisted electrochemical reduction of nitrogen to ammonia, *Chem. Commun.*, 2018, **54**(95), 13347–13350.
- 62 A. Togo and I. Tanaka, First principles phonon calculations in materials science, *Scr. Mater.*, 2015, **108**, 1–5.
- 63 V. Wang, *et al.*, VASPKIT: A user-friendly interface facilitating high-throughput computing and analysis using VASP code, *Comput. Phys. Commun.*, 2021, **267**, 108033.
- 64 D. Mirabelli, *et al.*, Is Mesothelioma Unrelated to the Lung Asbestos Burden? Comment on Visonà *et al.* Inorganic Fiber Lung Burden in Subjects with Occupational and/or Anthropogenic Environmental Asbestos Exposure in Broni (Pavia, Northern Italy): An SEM-EDS Study on Autoptic Samples, *International Journal of Environmental Research and Public Health*, 2021, **18**(13), 7177.
- 65 L. Espitia-Perez, *et al.*, Cytogenetic instability in populations with residential proximity to open-pit coal mine in Northern Colombia in relation to PM<sub>10</sub> and PM<sub>2.5</sub> levels, *Ecotoxicol. Environ. Saf.*, 2018, **148**, 453–466.
- 66 C. Teng, Y. Wang and J. L. Bao, Physical Prior Mean Function-Driven Gaussian Processes Search for Minimum-Energy Reaction Paths with a Climbing-Image Nudged Elastic Band: A General Method for Gas-Phase, Interfacial, and Bulk-Phase Reactions, *J. Chem. Theory Comput.*, 2024, 4308–4324.
- 67 E. L. Kolsbjerg, M. N. Groves and B. Hammer, An automated nudged elastic band method, *J. Chem. Phys.*, 2016, **145**(9), 094107.
- 68 X. Liu, *et al.*, Lattice thermal conductivity of two-dimensional CrB<sub>4</sub> and MoB<sub>4</sub> monolayers against Slack's guideline, *Results Phys.*, 2023, **51**, 106696.
- 69 M. Tahir, U. Burki and T. Azid, Terrorism and environmental sustainability: empirical evidence from the MENA region, *Resour. Environ. Sustain.*, 2022, **8**, 100056.
- 70 M. Shahiduzzaman, *et al.*, The benefits of ionic liquids for the fabrication of efficient and stable perovskite photovoltaics, *Chem. Eng. J.*, 2021, **411**, 128461.
- 71 X. Jiang, *et al.*, Ultralow thermal conductivity and anharmonic rattling in two-dimensional WB<sub>4</sub> monolayer, *Appl. Phys. Lett.*, 2022, **120**(13), 132202.
- 72 M. K. Masood, *et al.*, A novel two-dimensional whorled CrB<sub>4</sub> and MoB<sub>4</sub> as high-performance anode material for metal ion batteries, *Appl. Surf. Sci.*, 2024, 159301.
- 73 J. Gasparotto and K. D. B. Martinello, Coal as an energy source and its impacts on human health, *Energy Geosci.*, 2021, **2**(2), 113–120.
- 74 M. K. H. Rabaia, *et al.*, Environmental impacts of solar energy systems: A review, *Sci. Total Environ.*, 2021, **754**, 141989.
- 75 H. Barthélémy, M. Weber and F. Barbier, Hydrogen storage: Recent improvements and industrial perspectives, *Int. J. Hydrogen Energy*, 2017, **42**(11), 7254–7262.
- 76 H. B. Munawar, *et al.*, Structural, electronic, magnetic, and optical properties of MFe<sub>2</sub>O<sub>4</sub> (M= Ni, Fe, Co) spinel ferrites: A density functional theory study, *Int. J. Quantum Chem.*, 2023, e27124.
- 77 K. Bidai, *et al.*, First-principles calculations of pressure and temperature dependence of thermodynamic properties of anti-perovskite BiNb<sub>3</sub> compound, *Chin. J. Phys.*, 2017, **55**(5), 2144–2155.
- 78 M. Usman, *et al.*, First-principles calculations to investigate the effect of Cs-doping in BaTiO<sub>3</sub> for water-splitting application, *Solid State Commun.*, 2022, **355**, 114920.

- 79 A. Stamatelatos, *et al.*, Optical interpretation for plasmonic adjustment of nanostructured Ag-NiO thin films, *Int. J. Mod. Phys. B*, 2021, **35**(06), 2150093.
- 80 G. Barik and S. Pal, Monolayer Molybdenum Diborides containing Flat and Buckled Boride Layers as Anode Materials for Lithium-Ion Batteries, *Phys. Chem. Chem. Phys.*, 2023, (26), 17667–17679.
- 81 G. Barik and S. Pal, 2D MoS<sub>2</sub>-MoSe<sub>2</sub> and MoS<sub>2</sub>-NbS<sub>2</sub> lateral heterostructures as anode materials for LIBs/SIBs, *Appl. Surf. Sci.*, 2022, **596**, 153529.
- 82 G. Walker, Hydrogen storage technologies, in *Solid-state Hydrogen Storage*, Elsevier, 2008, pp. 3–17.
- 83 M. Born and K. Huang, *Dynamical Theory of Crystal Lattices*, Oxford university press, 1996.
- 84 G. Barik and S. Pal, Monolayer molybdenum diborides containing flat and buckled boride layers as anode materials for lithium-ion batteries, *Phys. Chem. Chem. Phys.*, 2023, **25**(26), 17667–17679.
- 85 S. Niaz, T. Manzoor and A. H. Pandith, Hydrogen storage: Materials, methods and perspectives, *Renewable Sustainable Energy Rev.*, 2015, **50**, 457–469.
- 86 Y. Kuai, *et al.*, Two-dimensional SiP<sub>3</sub> monolayer as promising anode with Record-high capacity and fast diffusion for Alkali-ion battery, *Appl. Surf. Sci.*, 2022, **586**, 152510.
- 87 Y. Kuai, *et al.*, A two-dimensional metallic SnB monolayer as an anode material for non-lithium-ion batteries, *Phys. Chem. Chem. Phys.*, 2022, **24**(38), 23737–23748.
- 88 N. Khossossi, *et al.*, Revealing the superlative electrochemical properties of o-B<sub>2</sub>N<sub>2</sub> monolayer in Lithium/Sodium-ion batteries, *Nano Energy*, 2022, **96**, 107066.
- 89 J. Tao and L. Guan, Tailoring the electronic and magnetic properties of monolayer SnO by B, C, N, O and F adatoms, *Sci. Rep.*, 2017, **7**(1), 1–7.
- 90 D. Er, *et al.*, Ti<sub>3</sub>C<sub>2</sub> MXene as a high capacity electrode material for metal (Li, Na, K, Ca) ion batteries, *ACS Appl. Mater. Interfaces*, 2014, **6**(14), 11173–11179.
- 91 Y. Wen, *et al.*, Expanded graphite as superior anode for sodium-ion batteries, *Nat. Commun.*, 2014, **5**(1), 4033.
- 92 S. Ahmad, *et al.*, First principles study of the adsorption of alkali metal ions (Li, Na, and K) on Janus WSSe monolayer for rechargeable metal-ion batteries, *Appl. Surf. Sci.*, 2023, **632**, 157545.
- 93 A. D. Becke and K. E. Edgecombe, A simple measure of electron localization in atomic and molecular systems, *J. Chem. Phys.*, 1990, **92**(9), 5397–5403.
- 94 C. Tarhan and M. A. Çil, A study on hydrogen, the clean energy of the future: Hydrogen storage methods, *J. Energy Storage*, 2021, **40**, 102676.
- 95 S. Karimzadeh, B. Safaei and T.-C. Jen, Investigation on electrochemical performance of striped,  $\beta$ 12 and  $\chi$ 3 Borophene as anode materials for lithium-ion batteries, *J. Mol. Graphics Modell.*, 2023, **120**, 108423.
- 96 J. Rehman, *et al.*, An overview of 2D metal sulfides and carbides as Na host materials for Na-ion batteries, *Chem. Eng. J.*, 2023, **461**, 141924.
- 97 M. K. Masood, *et al.*, Theoretical prediction of stable WB<sub>4</sub> monolayer as a high-capacity anode material for alkali-metal ion batteries, *J. Phys. Chem. Solids*, 2023, 111814.
- 98 B. Akgenc, New predicted two-dimensional MXenes and their structural, electronic and lattice dynamical properties, *Solid State Commun.*, 2019, **303**, 113739.
- 99 M. Li, *et al.*, A novel hyperbolic two-dimensional carbon material with an in-plane negative Poisson's ratio behavior and low-gap semiconductor characteristics, *ACS Omega*, 2020, **5**(26), 15783–15790.
- 100 C. Lundgren, A. Kakanakova-Georgieva and G. K. Gueorguiev, A perspective on thermal stability and mechanical properties of 2D Indium Bismide from ab initio molecular dynamics, *Nanotechnology*, 2022, **33**(33), 335706.
- 101 A. Ghosh, S. Pal and P. Sarkar, Rational design of two-dimensional porous boron phosphide as efficient cathode material for Li and Na ion batteries: a first-principles study, *J. Phys. Chem. C*, 2022, **126**(11), 5092–5100.
- 102 A. Ghosh, S. Mandal and P. Sarkar, 2D Homogeneous Holey Carbon Nitride: An Efficient Anode Material for Li-ion Batteries With Ultrahigh Capacity, *ChemPhysChem*, 2022, **23**(15), e202200182.
- 103 J. Vetter, *et al.*, Ageing mechanisms in lithium-ion batteries, *J. Power Sources*, 2005, **147**(1–2), 269–281.
- 104 X. Lv, *et al.*, Metallic FeSe monolayer as an anode material for Li and non-Li ion batteries: a DFT study, *Phys. Chem. Chem. Phys.*, 2020, **22**(16), 8902–8912.
- 105 R. A. Barreto, Fossil fuels, alternative energy and economic growth, *Econ. Modell.*, 2018, **75**, 196–220.
- 106 D. Wang, *et al.*, Robust vanadium pentoxide electrodes for sodium and calcium ion batteries: thermodynamic and diffusion mechanical insights, *J. Mater. Chem. A*, 2016, **4**(32), 12516–12525.
- 107 W. Jin and Z. Wang, Facet-dependent magnesianion behavior of  $\alpha$ -Sn as an anode for magnesium ion batteries, *RSC Adv.*, 2017, **7**(70), 44547–44551.
- 108 Y. Cao, *et al.*, *Density Functional Theory Calculations for the Evaluation of FePS<sub>3</sub> as a Promising Anode for Mg Ion Batteries*, Transactions of Tianjin University, 2020, vol. 26, pp. 248–255.
- 109 Y. Zhang, *et al.*, A novel highly stable two-dimensional boron phase with promising potentials in energy fields, *J. Mater. Chem. A*, 2023, **11**(2), 828–837.
- 110 Y. Wei, *et al.*, Effect of Oxygen Vacancies and F-Doping on TiO<sub>2</sub> (B) as Anode for Mg-Ion Batteries, *J. Phys. Chem. C*, 2023, **127**(29), 14086–14097.
- 111 J. Shuai, *et al.*, Density functional theory study of Li, Na, and Mg intercalation and diffusion in MoS<sub>2</sub> with controlled interlayer spacing, *Mater. Res. Express*, 2016, **3**(6), 064001.
- 112 X. Li, Y. Li and Y. Wang, Adsorption of Ca on borophene for potential anode for Ca-ion batteries, *J. Mol. Model.*, 2023, **29**(10), 308.
- 113 M. M. Kadhim, *et al.*, Study the application of nitrogenated holey graphene (C<sub>2</sub>N) nanosheets as a high-performance

- anode material for magnesium ion battery (MIB): DFT study, *Inorg. Chem. Commun.*, 2023, **148**, 110296.
- 114 Q. Gao, X.-J. Ye and C.-S. Liu, Monolayer  $\alpha$ -beryllene as an anode material for magnesium ion batteries with high capacity and low diffusion energy barrier, *Phys. Chem. Chem. Phys.*, 2023, **25**(8), 6519–6526.
- 115 M. I. Khan, *et al.*, A DFT study of bismuthene as anode material for alkali-metal (Li/Na/K)-ion batteries, *Mater. Sci. Eng.*, 2021, **266**, 115061.
- 116 M. I. Khan, *et al.*, A DFT study on a borophene/boron nitride interface for its application as an electrode, *Phys. Chem. Chem. Phys.*, 2020, **22**(6), 3304–3313.
- 117 M. A. Hadi, *et al.*, Evaluation of the role perfect and defect boron nitride monolayer in calcium ion batteries as a anode, *Comput. Theor. Chem.*, 2023, **1219**, 113940.
- 118 A. Emly and A. Van der Ven, Mg intercalation in layered and spinel host crystal structures for Mg batteries, *Inorg. Chem.*, 2015, **54**(9), 4394–4402.
- 119 C. Xiao, *et al.*, Graphene-like BSi as a promising anode material for Li-and Mg-ion batteries: A first principle study, *Appl. Surf. Sci.*, 2021, **563**, 150278.
- 120 Q. Meng, *et al.*, The S-functionalized Ti<sub>3</sub>C<sub>2</sub>Mxene as a high capacity electrode material for Na-ion batteries: a DFT study, *Nanoscale*, 2018, **10**(7), 3385–3392.
- 121 B. Liang, *et al.*, N-functionalized Ti<sub>2</sub>B MBene as high-performance anode materials for sodium-ion batteries: A DFT study, *Appl. Surf. Sci.*, 2022, **599**, 153927.
- 122 Y.-C. Rao, *et al.*, Prediction of MoO<sub>2</sub> as high capacity electrode material for (Na, K, Ca)-ion batteries, *Appl. Surf. Sci.*, 2019, **479**, 64–69.
- 123 D. Çakır, *et al.*, Mo<sub>2</sub>C as a high capacity anode material: A first-principles study, *J. Mater. Chem. A*, 2016, **4**(16), 6029–6035.
- 124 N. A. Jaber, *et al.*, BC<sub>2</sub>N nanotube as a promising anode for rechargeable calcium ion batteries, *Mater. Chem. Phys.*, 2023, **294**, 126926.
- 125 M. I. Khan, *et al.*, Computational studies of super-B as anodes for AM (Li, Na, and K) ion batteries, *J. Electrochem. Soc.*, 2022, **169**(9), 090514.
- 126 X. Han, *et al.*, Density functional theory calculations for evaluation of phosphorene as a potential anode material for magnesium batteries, *RSC Adv.*, 2018, **8**(13), 7196–7204.
- 127 Z. Yang, *et al.*, Nanostructures and lithium electrochemical reactivity of lithium titanites and titanium oxides: A review, *J. Power Sources*, 2009, **192**(2), 588–598.
- 128 A. Samad and U. Schwingenschlögl, M<sub>2</sub>X Monolayers as Anode Materials for Li Ion Batteries, *Phys. Rev. Appl.*, 2021, **15**(3), 034025.